



Cite as
Nano-Micro Lett.
(2024) 16:169

Received: 7 January 2024
Accepted: 24 February 2024
© The Author(s) 2024

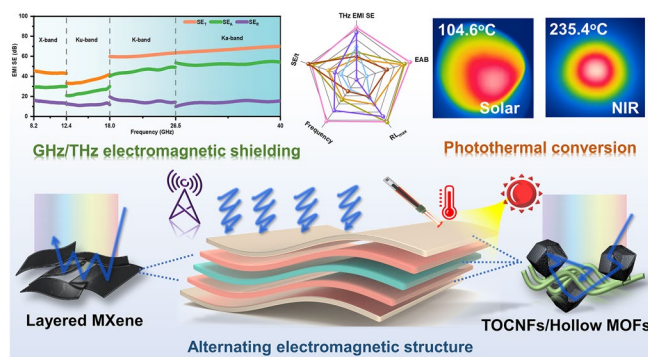
Hollow Metal–Organic Framework/MXene/ Nanocellulose Composite Films for Giga/Terahertz Electromagnetic Shielding and Photothermal Conversion

Tian Mai¹, Lei Chen¹, Pei-Lin Wang¹, Qi Liu¹, Ming-Guo Ma^{1,2}

HIGHLIGHTS

- The composite films are composed of hollow metal–organic frameworks/layered MXene/nanocellulose with unique alternating electromagnetic structures.
- The optimized composite films exhibit excellent EMI shielding performance of 66.8 dB at GHz frequency and 114.6 dB at THz frequency.
- The EMI shielding ability of composite films to electromagnetic waves is verified by practical visualized application simulation.
- The composite films show remarkable photothermal conversion performance, which can reach 235.4 °C under 0.8 W cm⁻².

ABSTRACT With the continuous advancement of communication technology, the escalating demand for electromagnetic shielding interference (EMI) materials with multifunctional and wideband EMI performance has become urgent. Controlling the electrical and magnetic components and designing the EMI material structure have attracted extensive interest, but remain a huge challenge. Herein, we reported the alternating electromagnetic structure composite films composed of hollow metal–organic frameworks/layered MXene/nanocellulose (HMN) by alternating vacuum-assisted filtration process. The HMN composite films exhibit excellent EMI shielding effectiveness performance in the GHz frequency (66.8 dB at Ka-band) and THz frequency (114.6 dB at 0.1–4.0 THz). Besides, the HMN composite films also exhibit a high reflection loss of 39.7 dB at 0.7 THz with an effective absorption bandwidth up to 2.1 THz. Moreover, HMN composite films show remarkable photothermal conversion performance, which can reach 104.6 °C under 2.0 Sun and 235.4 °C under 0.8 W cm⁻², respectively. The unique micro- and macro-structural design structures will absorb more incident electromagnetic waves via interfacial polarization/multiple scattering and produce more heat energy via the local surface plasmon resonance effect. These features make the HMN composite film a promising candidate for advanced EMI devices for future 6G communication and the protection of electronic equipment in cold environments.



KEYWORDS Metal–organic frameworks; MXene; Nanocellulose; Electromagnetic shielding; Photothermal conversion

✉ Ming-Guo Ma, mg_ma@bjfu.edu.cn

¹ Research Center of Biomass Clean Utilization, MOE Engineering Research Center of Forestry Biomass Materials and Bioenergy, Beijing Key Laboratory of Lignocellulosic Chemistry, College of Materials Science and Technology, Beijing Forestry University, Beijing 100083, People's Republic of China

² State Silica-Based Materials Laboratory of Anhui Province, Bengbu 233000, People's Republic of China

Published online: 08 April 2024



SHANGHAI JIAO TONG UNIVERSITY PRESS

Springer

1 Introduction

With the rapid development of modern science and technology, electronic devices have become ubiquitous in human daily life. However, electronic equipment brings convenience to our lives but also produces electromagnetic radiation pollution [1, 2]. As long as the electronic equipment is operating, it will produce electromagnetic radiation and affect the normal operation of the equipment, endangering human life and health [3, 4]. Especially in the 6G era, the frequency of electromagnetic wave bands used in communication expanded from GHz to THz, which undoubtedly aggravated the electromagnetic radiation pollution in the environment [5]. So, the development of electromagnetic protection materials is particularly important. Recently, cellulose-based electromagnetic protection materials have attracted wide attention [6]. Because of the abundant hydroxyl groups on the surface of cellulose, different functional groups can be obtained by modifying the hydroxyl group or cross-linking with functional materials through hydrogen bonding [7, 8]. Therefore, the selection of appropriate functional materials is the key to improving cellulose-based electromagnetic protection materials.

MXene was a new family in 2D material, which was first reported by Gogotsi's group in 2011 [9]. MXene has been found to have outstanding electromagnetic shielding performance due to its excellent electrical conductivity (≥ 10 times of reduced graphene oxide films) [10]. However, the development of MXene in the field of electromagnetic shielding materials is limited by a single electrical loss mechanism, which is limited by weak absorption attenuation, excessive conductivity, insufficient magnetic loss, and poor impedance matching performance [11]. Therefore, the development of electromagnetic shielding materials based on the electromagnetic double-loss mechanism is particularly important [12]. Metal-organic frameworks (MOFs) have the characteristics of low density, ordered structure, and rich adjustability. The metal nodes in MOFs will be reduced to metal nanoparticles, and the ligands will be converted into graphitized carbon after pyrolysis [13]. More importantly, due to the ordered structure, the metal nanoparticles will be doped in the graphitized carbon framework in a uniform distribution to avoid aggregation after pyrolysis. Therefore, MOFs-derived carbon materials are considered as excellent electromagnetic shielding materials. MOFs with high

permeability can complement the advantages of MXene with high conductivity [14]. However, doping lower conductive MOFs fillers directly into high conductive MXene will block the original conductive path, resulting in a sharp decline in conductivity, thus limiting the EMI performance of electromagnetic shielding materials [15].

The structural design of composite materials is also considered another effective way to adjust the impedance matching of electromagnetic waves at the interface by multiple reflections and scattering, thus improving the performance of EMI shielding effectiveness (EMI SE) and absorption efficiency [16]. Cao et al. [17] developed the carbon nanotubes/MXene/2,2,6,6-tetramethylpiperidine-1-oxyl oxidated cellulose nanofiber (TOCNFs) composite paper via a facile alternating vacuum-assisted filtration process with the EMI SE of 34.8 dB in the X band. The gradient sandwich structure regulates the contributions from reflection and absorption to effectively improve the performance of electromagnetic wave absorption efficiency of materials. Hu et al. [18] reported the asymmetric gradient structure CNFs/reduced graphene oxide/Fe₃O₄/silver nanowires nanocomposite film with the EMI SE from 63.1 to 112.9 dB in the X band. The unique asymmetric gradient structure can endow the composite with higher EMI SE via gradient absorption and gradient reflection in the layers. These works have greatly promoted the development of electromagnetic shielding films in structural design. However, the GHz and THz EMI research of multifunctional MOFs/MXene/nanocellulose composite films with unique gradient alternating electromagnetic structures have rarely been reported.

In this work, using TOCNFs as the polymer matrix, we fabricated MOFs-derived cobalt hollow carbon cage (Co-HCC) via in situ epitaxial growth and pyrolysis. Then, the hollow MOFs/layered MXene/nanocellulose (HMN) composite films with alternating electromagnetic structures were designed by the alternating vacuum-assisted filtration (AVAF) method. We explored that the alternating electromagnetic structure endows the GHz and THz electromagnetic wave transmission with a unique "alternating absorption-reflection" process, effectively improving the electromagnetic shielding performance. In addition, the practical EMI applications simulation of the HMN composite films was also investigated. More importantly, the excellent photothermal conversion ability also endows HMN composite films with the reliability of keeping electronic devices operating in cold

environments. This work proves that MOFs/MXene/nanocellulose composite films with alternating electromagnetic structures have potential applications in electronic warfare and electronic equipment anti-interference field.

2 Experimental Section

2.1 Materials

TEMPO-oxidized cellulose nanofibers (TOCNFs, 0.2 wt%) dispersion was purchased from Tianjin woodelfbio Co., Ltd. MAX Ti_3AlC_2 (99%, 400 mesh) was purchased from Jilin 11 Technology Co., Ltd. Lithium fluoride (LiF, 99%), 2-methylimidazole ($\text{C}_4\text{H}_6\text{N}_2$, 98.0%), cetyltrimethylammonium bromide (CTAB, 99%), and *N,N*-dimethylformamide (DMF, AR) were purchased from Shanghai Macklin Biochemical Technology Co., Ltd. Cobaltous nitrate hexahydrate (AR) and zinc nitrate hexahydrate (AR) were obtained from Guangzhou Huada Chemical Reagent Co., Ltd. Methanol (AR) and concentrated hydrochloric acid (HCl) were supplied by Beijing Modern Oriental Fine Chemistry Co., Ltd. The above chemicals were used without further purification. Filter membranes (cellulose, 0.45 μm pore size) were supplied by Tianjin Jinteng Experiment Equipment Co., Ltd.

2.2 Synthesis of Hollow Metal–Organic Frameworks

The synthesis process is based on a previous report [19]. For the synthesis of ZIF-8, the 0.02 mol zinc nitrate hexahydrate and 0.075 mol $\text{C}_4\text{H}_6\text{N}_2$ were dissolved in 100 mL methanol, respectively. The $\text{C}_4\text{H}_6\text{N}_2$ then slowly dripped into the zinc nitrate solution hexahydrate solution. The solution was mixed and stirred at room temperature for 24 h. Subsequently, the white precipitate was collected by centrifugation with methanol and DMF several times to remove the remaining chemicals and replace fresh solvents each time, followed by vacuum-drying at 80 °C overnight. For the synthesis of ZIF-67, 0.02 mol cobalt nitrate hexahydrate and 0.075 mol $\text{C}_4\text{H}_6\text{N}_2$ were dissolved in 100 mL methanol, respectively. The subsequent processing method is similar as the synthesis of ZIF-8. For the synthesis of ZIF-8@ZIF-67, 0.5 g ZIF-8 was dispersed in 100 mL methanol solution containing 0.02 mol cobalt nitrate hexahydrate. Then, 100 mL methanol solution containing 0.075 mol $\text{C}_4\text{H}_6\text{N}_2$ was further slowly

dripped into the above mixture. The subsequent processing method is similar as the synthesis of ZIF-8. The pyrolysis process was carried out in a tube furnace at a heating rate of 2 min^{-1} to 800 °C (maintained at 800 °C for 2 h) under nitrogen atmosphere to obtain the Co–HCC nanoparticles.

2.3 Synthesis of Delaminated $\text{Ti}_3\text{C}_2\text{T}_x$ MXene Nanosheets

Specifically, 1 g of LiF was added in 20 mL diluted HCl (9 M). Then, 1 g of Ti_3AlC_2 was slowly added into the HCl solution and kept stirring at 36 °C for 48 h and centrifuged with deionized water several times to obtain the multiple layers of $\text{Ti}_3\text{C}_2\text{T}_x$ (m- $\text{Ti}_3\text{C}_2\text{T}_x$). Finally, the m- $\text{Ti}_3\text{C}_2\text{T}_x$ was exfoliated via ultrasound under the ice bath and then centrifuged again. The obtained product is the delaminated $\text{Ti}_3\text{C}_2\text{T}_x$ (d- $\text{Ti}_3\text{C}_2\text{T}_x$).

2.4 Preparation of Hollow Metal Organic Frameworks/MXene/Nanocellulose (HMN) Composite Films

HMN composite films were prepared by the alternating vacuum-assisted filtration (AVAF) method. First, the surface of Co-HCC was modified with cationic surfactant CTAB (10 wt% based on Co-HCC) by mechanical stirring for 30 min [20]. Then, the dried Co-HCC was dispersed in TOCNFs suspension with ultrasonicated and mechanical stirred well-distributed. Herein, the mass ratio of TOCNFs and Co-HCC is controlled at 2:1. Then, the homogeneously suspended solution was vacuum-filtrated onto a cellulose filter membrane to form stable films. Subsequently, the d- $\text{Ti}_3\text{C}_2\text{T}_x$ suspension was vacuum filtrated on top of TOCNFs/Co-HCC to form stable films. Then repeat the above vacuum-filtrated steps to construct the gradient alternating electromagnetic structure. The HMN composite films with different total layers and d- $\text{Ti}_3\text{C}_2\text{T}_x$ content are named HMN-mL-*n*% (m means the total number of layers, and *n* means the d- $\text{Ti}_3\text{C}_2\text{T}_x$ content). The component content of each layer controls the gradient ratio change. For example, HMN-5L-57.1 wt% means that the total number of layers of composite films is five, including two d- $\text{Ti}_3\text{C}_2\text{T}_x$ layers and three TOCNFs/Co-HCC layers. The composition table is displayed in Tables S4–S7. After vacuum filtration, the obtained HMN composite films were dried at 50 °C in vacuum oven overnight and then carefully peeled off.

2.5 Characterization

The microstructure of composites was investigated by scanning electron microscope (SEM, ZEISS Gemini SEM 300, Germany), transmission electron microscope (TEM, JEM-2100 Plus, Japan) equipped with an energy-dispersive spectroscopy (EDS). The infrared spectra of samples were measured on a Fourier transform infrared spectrometer (FTIR, Thermo Scientific Nicolet iS5, USA). The surface chemistries of the samples were characterized by X-ray photoelectron spectroscopy (XPS, Thermo Scientific K-Alpha, USA). Raman spectra were performed on a laser Raman spectrometer with a 633-nm line laser as the excitation source (Horiba LabRAM HR Evolution, Japan). The phase structures of the composites were characterized by X-ray diffractometer (XRD, Rigaku Ultima IV, Japan). Thermal gravimetric analysis (TGA) was performed using a thermogravimetric analyzer (TA STD Q600, USA). Brunauer–Emmett–Teller (BET, ASAP 2460, USA) analysis measured the specific surface area. Zeta-potentials (Malvern Zetasizer Nano ZS90, Britain) were measured in de-ionized water. The electromagnetic radiation detector (LZT-1000, China) was used to detect the electromagnetic radiation of the Tesla coil. The electrical conductivity was tested with Suzhou Jingge Electronic Four Probe Tester (ST2258C, China). The mechanical performance of materials was tested by an electronic universal testing machine (Instron 5943, USA). The tensile samples (20 mm long and 10 mm wide) were tested at a constant tensile rate of 0.2 mm min⁻¹. The magnetic hysteresis loop was measured by the vibrating sample magnetometer (VSM, BKT-4700, China). The relative permeability was calculated as follows:

$$\mu_r = \frac{(\& + 1)}{\mu_0} \quad (1)$$

where $\&$, μ_r , and μ_0 are magnetic susceptibility, relative permeability, and vacuum permeability. $\mu_0 = 4\pi \times 10^{-7}$ H m⁻¹.

The EMI shielding effectiveness (EMI SE) of samples was measured on the vector network analyzer (Agilent PNA-N5244A, USA) based on the S parameters. All composite films were cut to the size suitable for the test mold. For the frequency of 8.2–12.4 GHz, the sample size is 22.9 × 10.20 mm². For the frequency of 12.4–18 GHz, the sample size is 15.9 × 8.03 mm². For the frequency of 18.0–26.5 GHz, the sample size is 10.95 × 4.50 mm². For the frequency of

26.5–40 GHz, the sample size is 7.15 × 3.60 mm². Then the cut sample is firmly fixed in the cavity of the test mold. All the powder samples were mixed with melted paraffin, and the samples with suitable dimensions (inner 3.04 mm, outer 7.0 mm) were prepared at the mass ratio of powder to paraffin of 1:3 and tested in 8.2–12.4 GHz. Then the mixed paraffin sample is firmly fixed in the cavity of the test mold. The power of the vector network analyzer is set as -3 dBm, and the intermediate frequency bandwidth is set as 300 Hz.

The GHz EMI SE was calculated as follows:

$$SE_T = SE_R + SE_A \quad (2)$$

$$SE_T = 10 \times \log_{10} \left(\frac{1}{|S_{21}|^2} \right) \quad (3)$$

$$SE_R = 10 \times \log_{10} \left(\frac{1}{1 - |S_{11}|^2} \right) \quad (4)$$

$$SE_A = 10 \times \log_{10} \left(\frac{1 - |S_{11}|^2}{|S_{21}|^2} \right) \quad (5)$$

$$SE/t = \frac{\text{EMI SE}}{\text{thickness}} = \text{dB} \mu\text{m}^{-1} \quad (6)$$

$$SE/t = \frac{\text{EMI SE}}{\text{thickness} \times \text{density}} = \text{dB cm}^2 \text{g}^{-1} \quad (7)$$

where SE_T , SE_R , and SE_A are the GHz EMI SE, absorption of EMI SE, and reflection of EMI SE, respectively. SE/t is the thickness specific shielding effectiveness. SSE/t is specific shielding effectiveness [21, 22].

Terahertz time-domain spectroscopy measured the THz signals in the transmission mode system (Teraview Tera-Pulse Lx, Britain) and reflection mode system (Advantest TAS7400TS, Japan). The terahertz imaging was obtained by TAS7 × 00 2D Mapping Excel Macro R1.03. All composite films were cut to the size of 20 × 20 mm² suitable for the test mold and placed on a THz hollow circular (pore diameter is 12 mm) sample placement. The THz EMI SE was calculated as follows:

$$\text{THz EMI SE} = -20 \times \log_{10} \left(\frac{E_s}{E_a} \right) \quad (8)$$

$$R_L = -20 \times \log_{10} \left(\frac{E_r}{E_i} \right) \tag{9}$$

where E_s , E_a , R_L , E_r , and E_i are transmission terahertz electric field intensity for the samples, transmission terahertz electric field intensity for the air cavity, terahertz reflection loss, the amplitude intensity of the reflection signal of the samples, the amplitude intensity of the reflection signal of the aluminum mirror [23].

The UV–Vis–NIR absorbance spectrum was obtained by the UV–visible–near-infrared spectrophotometer (Shimadzu UV-3600i Plus, Japan). The infrared emissivity was tested by infrared emissivity tester (TSS-5X, Japan). The surface temperature of the samples was monitored by the infrared thermal imaging camera (Fotric 226, China). The 808-nm NIR laser (Shanghai Connect Fibre Optics Co., Ltd, China) and a Xenon lamp (PL-X500D, Beijing Precise Technology Co., Ltd, China) were used in experiment. The solar-to-thermal energy conversion efficiencies (η) of the samples were calculated as follows:

$$\eta = \frac{H_{in} - H_{loss}}{H_{in}} = \alpha - \frac{\epsilon \sigma (T^4 - T_r^4)}{I_{solar}} \tag{10}$$

where H_{in} is the energy input, H_{loss} is the energy loss, the α is the solar absorptivity, the ϵ represents the infrared emissivity, the T is the temperature of HMN composite films and T_r is room temperature, the σ points the Stefan–Boltzmann constant, the I_{solar} represents the power density of the incident sunlight [24].

3 Results and Discussion

3.1 Synthesis and Microstructure of HMN Composite Films

The synthesis of HMN composite films is illustrated in Fig. 1. Generally speaking, the hollow Co-HCC was mixed with TOCNFs suspension and then vacuum-filtrated on the cellulose filter membrane. After that, the d-Ti₃C₂T_x suspension was vacuum-filtrated on top of TOCNFs/Co-HCC. Finally, the above step is repeated repeatedly until stable HMN composite films are formed. Specifically, the ZIF-8@ZIF-67 with shell-core structure was prepared by *in situ* epitaxial growth. The ZIF-8 was used as the core, attracting Co²⁺ on its surface through electrostatic interaction (Fig. 1a). Organic ligand C₄H₆N₂ was then added to facilitate

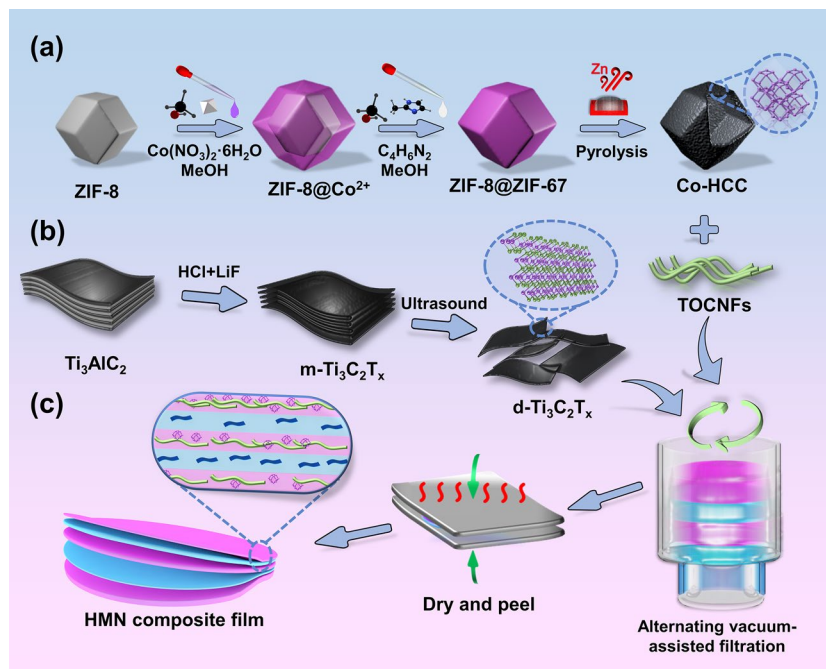


Fig. 1 Schematic diagrams of synthesis of HMN composite films by AVAF strategy. The fabrication process of **a** Co-HCC, **b** d-Ti₃C₂T_x, and **c** HMN composite films

the growth of ZIF-67 on the surface. As shown in Fig. S1, ZIF-8@ZIF-67 displays the classic rhombic dodecahedron structure as the same as ZIF-8. The particle size of ZIF-8@ZIF-67 (about 1.4 μm) is larger than that of ZIF-8 (about 1.0 μm), attributed to the epitaxial growth of ZIF-67 on the surface of ZIF-8. For further evidence of the shell-core structure of the as-prepared ZIF-8@ZIF-67, EDS line scanning reveals that Zn resides predominantly in the “central core,” while Co is mainly concentrated in the “outer shell” (Fig. S2). The unique core-shell structure makes ZIF-8@ZIF-67 form a hollow structure after pyrolysis. To avoid excessive collapse of the ZIF-8@ZIF-67 structure, 800 $^{\circ}\text{C}$ was selected as the calcination temperature [25, 26]. The imidazole ligand of ZIF-8@ZIF-67 was transformed into highly graphitized carbon, and the cobalt metal nodes of ZIF-67 were reduced. Due to the low boiling point of zinc, metal nodes within ZIF-8 will be gradually selectively evaporated away at high temperature (~ 800 $^{\circ}\text{C}$) from the “central core” during pyrolysis [27].

As shown in Fig. 2a, the Co-HCC shows the shape of the hollow polyhedron with the size of about 1.2 μm , and

the shrinkage of the size is caused by the inevitable partial collapse of the ZIFs material during pyrolysis, which is consistent with the results reported in the previous literature [28]. During the pyrolysis at high temperature, the flowing gas promotes the outward movement of metal ions and the formation of the hollow polyhedron. Besides, many CNTs are anchored on the rough surface of Co-HCC. The formation of CNTs on the surface is mainly due to the catalysis of Co nanoparticles and the evaporation of Zn [29]. Correspondingly the 0.20 nm lattice fringe with a spacing was assigned to the (111) crystal face of Co, and 0.36 nm was assigned to the (002) crystal face of highly graphitized carbon (Fig. S3) [30]. Furthermore, as displayed in Figs. 2b and S4, the EDS line scanning image and mapping exhibited the hollow structure of Co-HCC, Co is mainly distributed in the “outer shell,” and the “hollow core” is the graphite carbon of the organic ligand from carbonized ZIF-8. In addition, the signal intensity of the Zn element is slight in the whole image, which further proves that Zn is evaporated during pyrolysis. Moreover, Co-HCC also shows obvious magnetism and

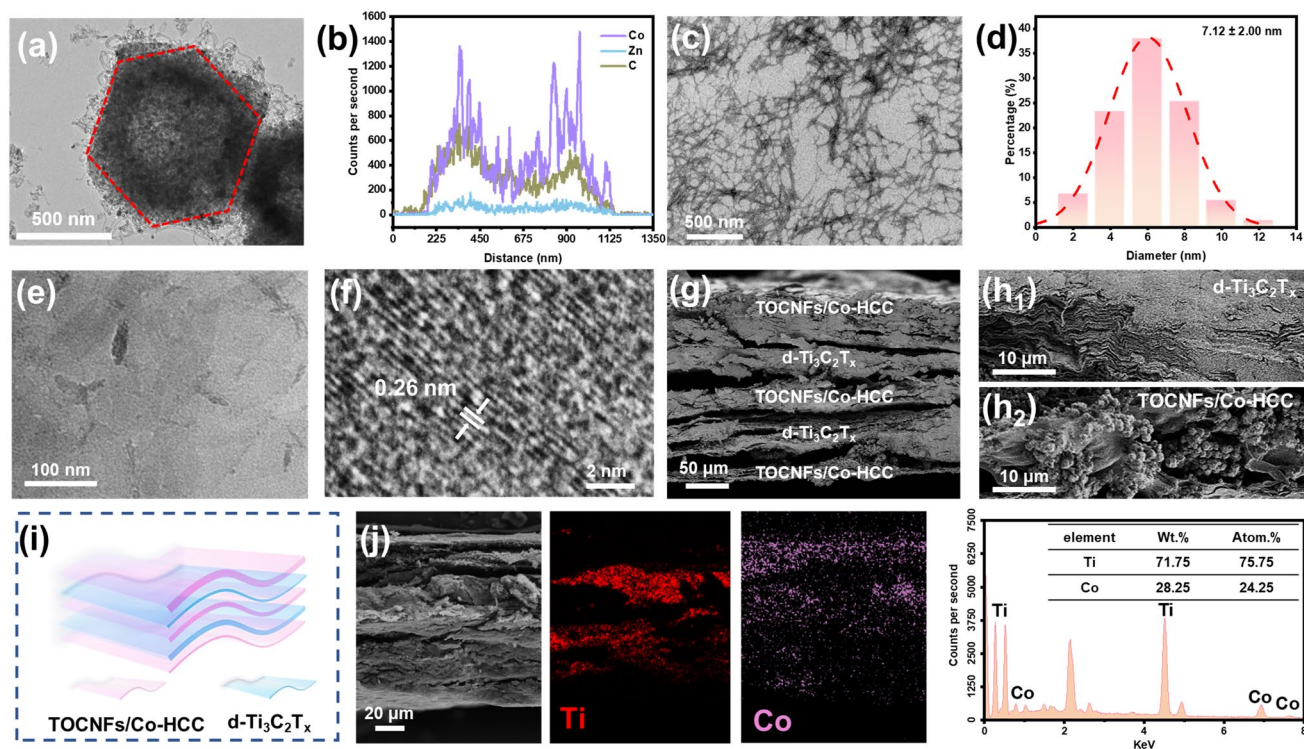


Fig. 2 Microstructure of the HMN composite films. **a** TEM image and **b** EDS line scanning image of Co-HCC, respectively. **c** TEM image and **d** size distribution of TOCNFs, respectively. **e** TEM image and **f** lattice fringe of $d\text{-Ti}_3\text{C}_2\text{T}_x$ nanosheets, respectively. **g**, **h** SEM image, **i** schematic illustration, and **j** EDS mapping of HMN composite films

can be attracted by magnets (Fig. S5a). TEM images show that the diameter of the TOCNF measures approximately 7.12 ± 2.00 nm, whereas its length is to be at the micrometer level (Fig. 2c, d). The high aspect ratio can easily lead to physical entanglement between TOCNFs and form a stable structure [31]. The diagram of the fabrication process of $d\text{-Ti}_3\text{C}_2\text{T}_x$ is displayed in Fig. 1b. A mild etching method was employed using LiF and hydrochloric acid as etchants to selectively etch the Al layer in the MAX Ti_3AlC_2 phase, resulting in the formation of accordion-shaped $m\text{-Ti}_3\text{C}_2\text{T}_x$, which was then further processed to obtain $d\text{-Ti}_3\text{C}_2\text{T}_x$ through ultrasonic delamination (Fig. 2e, f). Moreover, both the suspension of $d\text{-Ti}_3\text{C}_2\text{T}_x$ and TOCNFs displayed a distinct Tyndall effect when exposed to laser pointer irradiation, indicating the colloidal nature of the solutions prepared (Fig. S5b, c). In the AVAF process, Co-HCC was modified with cetyltrimethylammonium bromide (CTAB) and then dispersed into a TOCNFs suspension. After CTAB modification, the electro-positivity of Co-HCC is improved, which is helpful in generating electrostatic interaction with TOCNFs and $d\text{-Ti}_3\text{C}_2\text{T}_x$ to connect them closely (Fig. S6) [32]. Next, the resulting TOCNFs/Co-HCC solution was stirred and ultrasound to full uniformity. The TOCNFs/Co-HCC mixture was then vacuum-filtered onto a cellulose filter membrane. The $d\text{-Ti}_3\text{C}_2\text{T}_x$ solution is then vacuum-filtered at the top of TOCNFs/Co-HCC. The above steps are repeated to form a stable film structure (Fig. 1c). Finally, the HMN composite films were dried and peeled off from the cellulose filter membrane. As seen from Fig. 2g–i, HMN composite films have apparent gradient alternating structure. The $d\text{-Ti}_3\text{C}_2\text{T}_x$ presents the layered structure, while TOCNFs/Co-HCC presents the shish kebab structures. Besides, it can be seen from the EDS spectrum that the Ti element in $d\text{-Ti}_3\text{C}_2\text{T}_x$ and the Co element in Co-HCC are mainly divided into each layer. There is slight infiltration between layers, which is formed by the close connection between different layers, which is helpful in forming a stable film structure (Fig. 2j). The results further prove that the AVAF method can form gradient alternating structures composite films, which helps to give play to the respective advantages of different components in a whole material.

3.2 Characterization of Crystallographic Structure and Composition of the HMN Composite Films

The crystallographic structure and phase composition of the resultant HMN composite films were further explored. As shown in Fig. S7a, all ZIF-8@ZIF-67, ZIF-8, and ZIF-67 exhibit a series of similar characteristic peaks in the range of $5^\circ\text{--}35^\circ$, which explains that ZIF-8@ZIF-67 with shell-core structure prepared by epitaxial growth method can effectively retain the crystal properties of ZIF-8 and ZIF-67 [33]. After pyrolysis, the XRD characteristic peaks of ZIF-8@ZIF-67 disappeared and transformed into three characteristic peaks (44.2° , 51.5° , and 75.9°) of Co corresponded to (111), (200), and (220) planes with cubic structure. Besides, the characteristic peak (26.6°) of graphite carbon has corresponded to (002) plane (Fig. 3a). These prove that the Co metal node in the shell ZIF-67 has been successfully reduced to metal Co, and the organic ligand of ZIF-8@ZIF-67 is transformed into graphite carbon, which is consistent with the previous report [34]. Additionally, as displayed in Fig. 3b, the phenomenon can also be proved by the new peaks (Co–O, D band, G band, and 2D band) of Co-HCC in the Raman spectrum, compared with ZIF-8@ZIF-67 [35]. As shown in Figs. 3c and S7b, from the XRD pattern, two characteristic diffraction peaks ($2\theta = 15.0$ and 22.5°) were assigned to (101) and (002) crystal planes of TOCNFs. In addition, the characteristic (002) peak of $d\text{-Ti}_3\text{C}_2\text{T}_x$ shifts from $2\theta = 7.1^\circ$ to 6.0° , proving the interconnection between TOCNFs/Co-HCC and $d\text{-Ti}_3\text{C}_2\text{T}_x$ [36].

Besides, the above characteristic peaks are apparent in the HMN composite films, which prove the successful preparation of the composite materials. To further explore the components of HMN composite films, the FTIR spectrum is displayed in Fig. 3d. The characteristic peaks of TOCNFs were observed at 1050 and 1600 cm^{-1} , attributing to the stretching vibration of the C–O–C group of the glucopyranose ring and the existence of the carbonyl [37]. The Ti_3AlC_2 where no particular peak can be detected in the FTIR spectrum, depicts the purity of MAX. The $d\text{-Ti}_3\text{C}_2\text{T}_x$ shows peaks at 580 and 1380 cm^{-1} that correspond to –OH and C–F groups. Besides, all ZIF-67, ZIF-8, and ZIF-8@ZIF-67 present several characteristic peaks in the range of $500\text{--}2000\text{ cm}^{-1}$ (Fig. S8). After carbonization at high

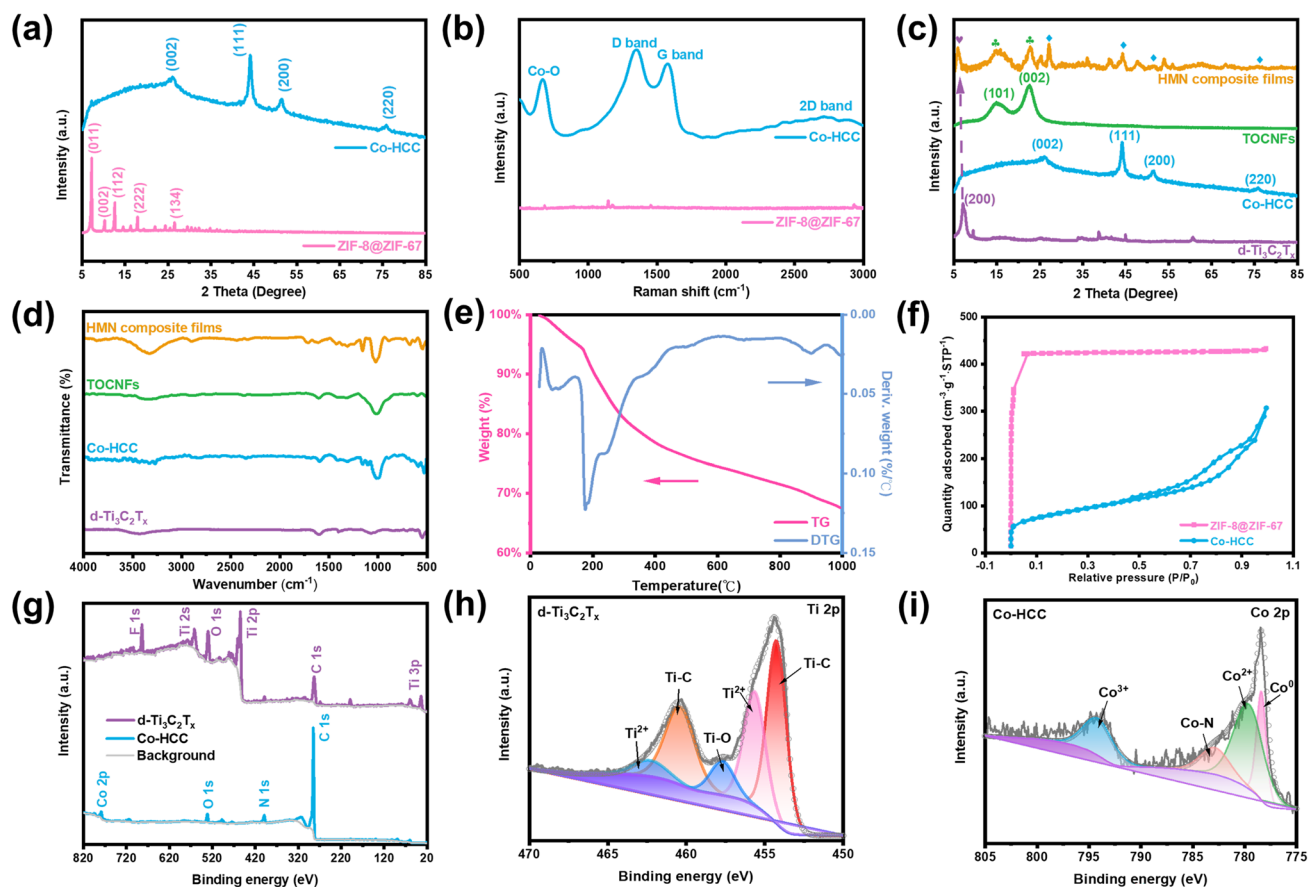


Fig. 3 The crystallographic structure and composition of the HMN composite films. **a** XRD patterns and **b** Raman patterns of ZIF-8@ZIF-67 before and after pyrolysis, respectively. **c** XRD patterns and **d** FTIR spectra of HMN composite films, TOCNFs, Co-HCC, and $d\text{-Ti}_3\text{C}_2\text{T}_x$, respectively. **e** TG and DTG analysis of HMN composite films. **f** The nitrogen adsorption–desorption isotherms of ZIF-8@ZIF-67 and Co-HCC. **g** XPS full spectra of $d\text{-Ti}_3\text{C}_2\text{T}_x$ and Co-HCC. XPS fine spectra of **h** Ti 2p of $d\text{-Ti}_3\text{C}_2\text{T}_x$ and **i** Co 2p of Co-HCC

temperature, the two new peaks remain at 560 and 650 cm^{-1} , corresponding to Co [38]. These characteristic peaks were also observed in the FTIR spectrum of HMN composite films. TGA and DTG were used to analyze the composition of HMN composite films (Fig. 3e). The decline curve of TG accords with cellulose. The high residual weight percentage is attributed to $d\text{-Ti}_3\text{C}_2\text{T}_x$ derivative titanium dioxide at high temperature and Co-HCC [39, 40]. The specific surface areas and N_2 absorption–desorption of ZIF-8@ZIF-67 and Co-HCC were researched (Figs. 3f and S9a). N_2 absorption–desorption results show that saturation is achieved at low relative pressure for the ZIF-8@ZIF-67, demonstrating the microporous structure of the materials with the typical type I adsorption–desorption isotherms. The specific surface area of ZIF-8@ZIF-67 reached 1565.6 and $1862.9\text{ m}^2\text{ g}^{-1}$ in the BET model and Langmuir model, respectively. By

contrast, the isotherms of Co-HCC show a relatively low N_2 absorption–desorption capacity and specific surface area (297.7 and $920.7\text{ m}^2\text{ g}^{-1}$ in the BET model and Langmuir model, respectively), probably caused by partial collapse of the frame. The typical type IV and the H3 hysteresis loop of Co-HCC exhibited the generation of hollow structure of materials [41]. Moreover, the average pore size (1.71 nm) of ZIF-8@ZIF-67 was less than the average pore size (6.38 nm) of Co-HCC. The pore size and pore volume of Co-HCC increased and gradually deviated from the microporous structure, which proved the hollow structure of Co-HCC (Figs. S9b and S10). The XPS analysis was used to further investigate the chemical compositions of $d\text{-Ti}_3\text{C}_2\text{T}_x$ and Co-HCC (Fig. 3g–i). The XPS spectra show that the $d\text{-Ti}_3\text{C}_2\text{T}_x$ and Co-HCC contain C, O, Ti, F, and C, O, N, Co elements, respectively. In the Ti 2p spectrum, a series of characteristic

peaks for Ti–C, Ti–O, and Ti²⁺ were detected, thereby corroborating the existence of surface partial oxidation on the d-Ti₃C₂T_x [42]. In the Co 2p spectrum, a series of characteristic peaks for Co⁰, Co²⁺, and Co³⁺ suggest the presence of metallic Co⁰, cobalt oxide, and cobalt tetroxide in the Co-HCC [40]. Besides, as shown in Fig. S11, the XPS fine spectrum of the N 1s peak was deconvoluted into four peaks, including oxidized-N, graphitic N, Co–N, and pyridinic N, respectively. In addition, the rich N element is helpful in improving the electromagnetic shielding performance of the materials [43]. The XPS fine spectra of Zn 2p indicated a doublet peak fitted at 1022.0 and 1045.1 eV attributed to Zn 2p_{3/2} and Zn 2p_{1/2}. The binding energy difference between

these observed Zn 2p_{3/2} and Zn 2p_{1/2} peaks about 23.1 eV, which is the same as the standard reference peaks value of the ZnO (Fig. S12) [44].

3.3 Electromagnetic Properties and Giga/Terahertz Electromagnetic Shielding Performances of HMN Composite Films

Electrical conductivity and permeability are crucial in determining the EMI shielding properties. The electrical and magnetic characteristics of HMN composite films are shown in Figs. 4a, b and S13. Interestingly, the unique structural design endows the HMN composite films with

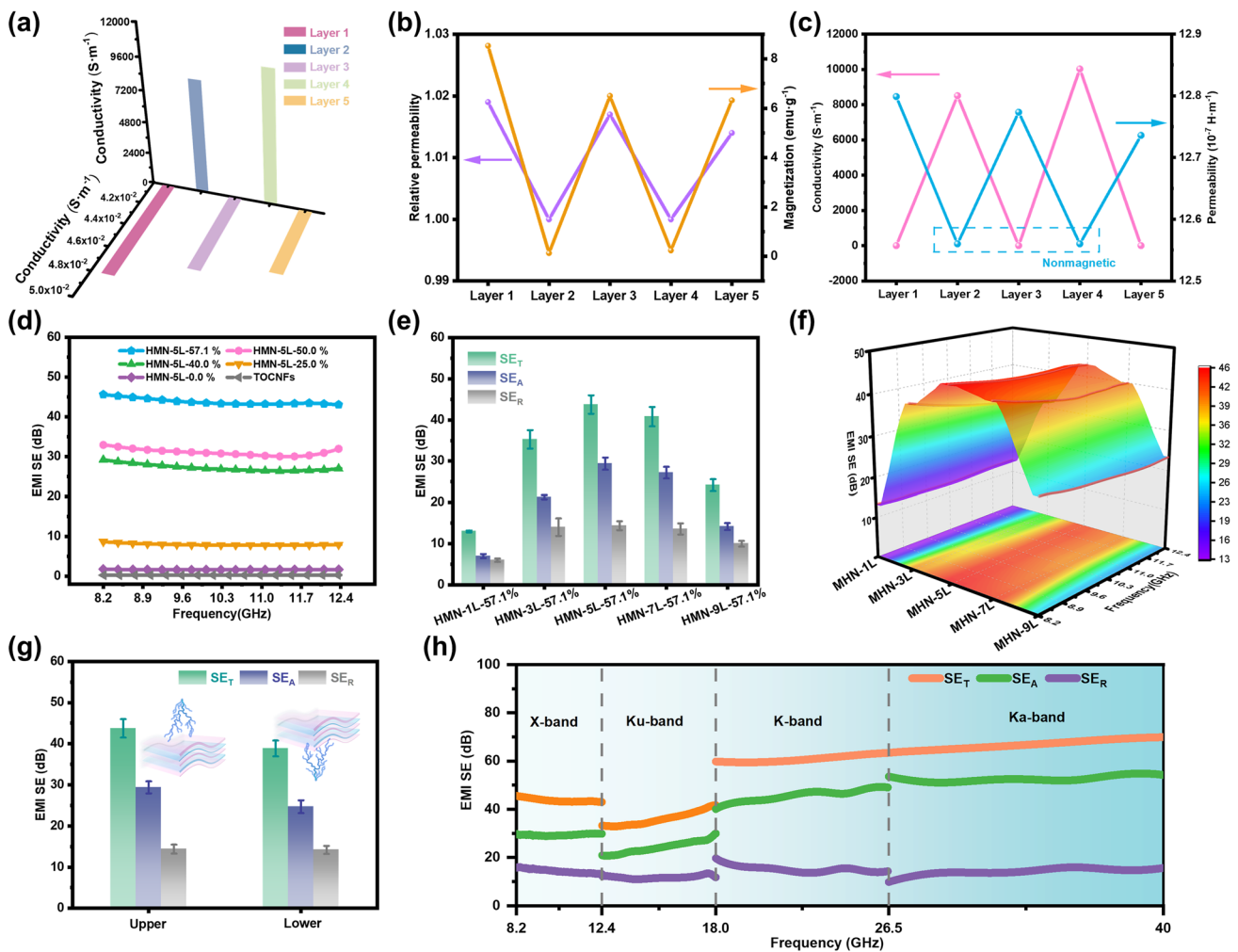


Fig. 4 Electromagnetic properties and gigahertz electromagnetic shielding performances of HMN composite films. **a–c** Conductivity and magnetism of HMN-5L-57.1% composite films. **d** EMI SE of HMN composite films with different d-Ti₃C₂T_x contents. **e, f** EMI SE of HMN composite films with different numbers of layers. **g** Schematic diagram and EMI SE of HMN-5L-57.1% composite films when the electromagnetic waves are incident from different directions, respectively. **h** X, Ku, K, and Ka-band EMI SE of HMN-5L-57.1% composite films

unique electromagnetic structure because the contents of Co-HCC, MXene, and TOCNFs in each layer are different in the process of preparing HMN composite films and the electromagnetic properties of each layer will be different after TVAF process. Therefore, HMN composite films present an electromagnetic structure with gradient alternation. The total saturation magnetization of HMN composite film is 5.00 emu g^{-1} . The first, third, and fifth layers are TOCNFs/Co-HCC layers with decreasing saturation magnetic induction (8.53 , 6.50 , and 6.32 emu g^{-1}). The second and fourth layers are $\text{d-Ti}_3\text{C}_2\text{T}_x$ layers with increasing electrical conductivity (8503.5 and $10,021.1 \text{ S m}^{-1}$), which is greater than the minimum requirement for electromagnetic shielding performance (1 S m^{-1}) [45]. As can be seen from Fig. 4c, the electrical conductivity and saturation magnetic induction of different layers in the composite film show an alternating increasing and decreasing trend. The conductive substance in the composite is mainly $\text{d-Ti}_3\text{C}_2\text{T}_x$, while the magnetic substance is mainly Co-HCC nanoparticles. The saturation magnetization between different layers of HMN composite films shows an alternating trend of "strong–weak–strong–weak–strong," while the electrical conductivity shows an alternating trend of "low–high–low–high–low." This alternating electromagnetic structure contributes to the loss of electromagnetic waves inside the HMN composite films. The electromagnetic waves will produce interface loss between components with different conductivity and permeability, and orderly electromagnetic structure design components will also make it difficult for electromagnetic waves to penetrate the whole materials [46]. The vector network analyzer is used to measure the S parameters of GHz electromagnetic waves before and after passing through the samples (Fig. S14). To further prove the loss effect of materials on electromagnetic waves, the EMI SE of ZIF-8@ZIF-67, Co-HCC, and $\text{d-Ti}_3\text{C}_2\text{T}_x$ was measured. ZIF-8@ZIF-67 exhibits negligible loss in its ability to mitigate electromagnetic waves due to the electrical and magnetic insulation properties. Conversely, Co-HCC exhibits a certain level of magnetic and electrical conductivity, thereby endowing it with the capacity to reflect and absorb electromagnetic waves. However, the relative lower conductivity impairs the EMI SE. The $\text{d-Ti}_3\text{C}_2\text{T}_x$ displays exceptional conductivity, enabling it to reflect a significant proportion of electromagnetic waves. Consequently, $\text{d-Ti}_3\text{C}_2\text{T}_x$ exhibits superior shielding performance while exhibiting a relatively low absorption value (Fig. S15). Therefore, structural design to fabricate

composite materials comprising high-magnetic Co-HCC and high-conductive $\text{d-Ti}_3\text{C}_2\text{T}_x$ is an approach that effectively enhances the overall performance of electromagnetic shielding materials. As can be seen in Fig. 4d, due to the high conductivity of $\text{d-Ti}_3\text{C}_2\text{T}_x$, the electromagnetic shielding performance of HMN composite films is also improved with the increasing content of $\text{d-Ti}_3\text{C}_2\text{T}_x$. When the content of $\text{d-Ti}_3\text{C}_2\text{T}_x$ is increased from 0 to 57.1%, the EMI SE is also increased from 1.71 to 45.6 dB. However, pure TOCNFs films have almost no electromagnetic shielding performance (0.2 dB). Although the HMN-5L-0% composite films contained Co-HCC, the electromagnetic shielding performance is also low (1.71 dB) because of its poor conductivity. Therefore, conductivity plays a leading role in EMI SE in electromagnetic shielding materials, which is consistent with previous report [47]. To prove the influence of electromagnetic separation multi-layer structure on electromagnetic shielding performance, HMN-nL-57.1% with a total number of n ($n = 1, 3, 5, 7, 9$) layers was designed according to gradient content (Fig. 4e, f). When all the components are mixed to form a random structure, the average EMI SE of HMN-1L-57.1% is only 13.0 dB, which cannot meet the lowest standard of commercial electromagnetic shielding materials (more than 20 dB) [48]. With the increase in the number of layers, the average EMI SE of HMN-3L-57.1% and HMN-5L-57.1% can reach 35.3 and 43.7 dB, respectively.

After the structural design, the electromagnetic shielding performance of HMN-5L-57.1% is 3.36 times that of HMN-1L-57.1% without changing the total composition of the composite films. Interestingly, with the further increase of the number of layers, the average EMI SE of HMN-7L-57.1% and HMN-9L-57.1% is 40.8 and 24.2 dB, respectively. The reason for this situation may be that when there are too many layers, the thickness between each layer is too low, which makes the mutual penetration of the electromagnetic components more serious, leading to the decline of electromagnetic shielding ability [49]. However, it is still greater than the electromagnetic shielding ability of HMN-1L-57.1% with random structure. In addition, the design of the gradient structure also endows HMN composite films with different electromagnetic shielding abilities on two sides. As shown in Fig. 4g, the electromagnetic shielding ability of forward incidence is higher than that of backward incidence, which is attributed to the result of different reflection and absorption of electromagnetic waves on the surfaces of different layers. This phenomenon can be attributed to

that when electromagnetic waves are incident from different layers of composite materials, it will affect the loss of electromagnetic waves in subsequent components, thus making the electromagnetic shielding performance different. Similar results have appeared in previous reports [50, 51]. Besides, to demonstrate the superiority of structural design, the electromagnetic shielding performance of MN composite films (without Co-HCC) and pure MXene films was evaluated (Figs. S16 and S17). The EMI SE and A coefficient of the HMN composite films were higher than MN composite films. This phenomenon further proves that the synergistic effect of Co-HCC magnetic loss and TOCNF scattering loss in the HMN composite films can improve the electromagnetic shielding performance [38]. The EMI SE of pure MXene films was slightly higher than HMN composite films, but the A coefficient was lower than HMN composite films. This is because pure MXene films have higher conductivity, which makes it have higher electromagnetic shielding ability, but it also brings the problem of impedance mismatch [31]. In order to further study the broadband EMI shielding performance of HMN composite films, the test electromagnetic frequency is extended to 40.0 GHz, including X-band (8.2–12.4 GHz), Ku-band (12.4–18 GHz), K-band (18–26.5 GHz), and Ka-band (26.5–40 GHz). As shown in Fig. 4h, HMN-5L-57.1% shows excellent average EMI SE in X-band (43.7 dB), Ku-band (36.0 dB), K-band (60.9 dB), and Ka-band (66.8 dB), which is beneficial to the individual requirements of electromagnetic shielding bands in different fields. Furthermore, the HMN composite films exhibited high absolute shielding effectiveness and thin thickness reaches up to $6534.1 \text{ dB cm}^2 \text{ g}^{-1}$ and $\sim 0.2 \text{ mm}$, which is envisaged for application within the electromagnetic shielding field of compact and mobile electronics apparatus (Fig. S18). In addition, the long-term stability of HMN composite films was also measured. Even after being stored at room temperature for 240 h, HMN composite films can still maintain 84.3% electromagnetic shielding performance (Fig. S19).

THz as an alternative electromagnetic wave band for future 6G communication, has higher frequency and energy, and its radiation to the human body cannot be ignored [52]. The electromagnetic shielding ability of HMN composite film at THz frequency is also researched. Terahertz time-domain spectroscopy is used to measure the signal and pattern changes of THz electromagnetic waves before and after passing through/reflecting the samples (Fig. S20). As displayed

in Fig. 5a, b in transmission mode, terahertz waves undergo significant attenuation when passing through HMN composite films, which proves that HMN composite films have strong shielding performance for terahertz waves. Because of the signal-to-noise ratio, porosity of the material, and the special functional relationship between the SE and frequency, the EMI SE part fluctuates in the whole THz range [18, 53, 54]. However, within the range of 0.1–4 THz, the averaging THz EMI SE is 114.6 dB (Fig. 5c). In addition, in the reflection mode, when terahertz waves contact the Al mirror, electromagnetic waves were reflected and exhibited a strong terahertz signal. And when contact with the HMN composite films, the obtained electromagnetic signals undergo significant attenuation, which proves that HMN composite film can effectively absorb THz electromagnetic waves (Fig. 5d, e). Within the range of 0.4–2.8 THz, the peak of reflecting electromagnetic waves reflection loss (R_L) has reached 39.7 dB at 0.6 THz, and the effective absorption bandwidth ($R_L > 10 \text{ dB}$) is up to 2.1 THz (Fig. 5f). Furthermore, THz imaging technology is utilized to visualize the shielding and absorbing ability of the composite films for THz waves. The THz imaging suggests that the terahertz wave signal undergoes precipitous attenuation post-contact with the HMN composite films. The aforementioned results validate that the HMN composite films possess good shielding and absorbing ability for terahertz waves (Fig. 5g, h).

As displayed in Fig. 6a, the EMI applications of HMN composite films were simulated visually. The electromagnetic field engendered by the Tesla coil renders it capable of serving as energy to stimulate a secondary coil (Fig. 6b). The high-frequency electromagnetic field is conveyed to the secondary coil via the radiation of the Tesla coil. Upon receipt of high-frequency electromagnetic radiation from the secondary coil, its charge becomes activated, causing electrons to transition and emanate energy, which is subsequently emitted in the form of luminescence, thus lighting the small bulb. The HMN composite films can obstruct the radiation, causing the small bulb to extinguish. However, the pure TOCNFs films cannot obstruct the radiation. Hence, the small bulb is still lighting (Movie S1). In addition, it can also be seen from the electromagnetic radiation detector that when the HMN composite films are blocked between the Tesla coil and the detector, the electromagnetic radiation alarm sound disappears, and when the films are removed, the alarm sound rings again (Fig. 6c, d and Movie S2). The EMI shielding mechanism of HMN

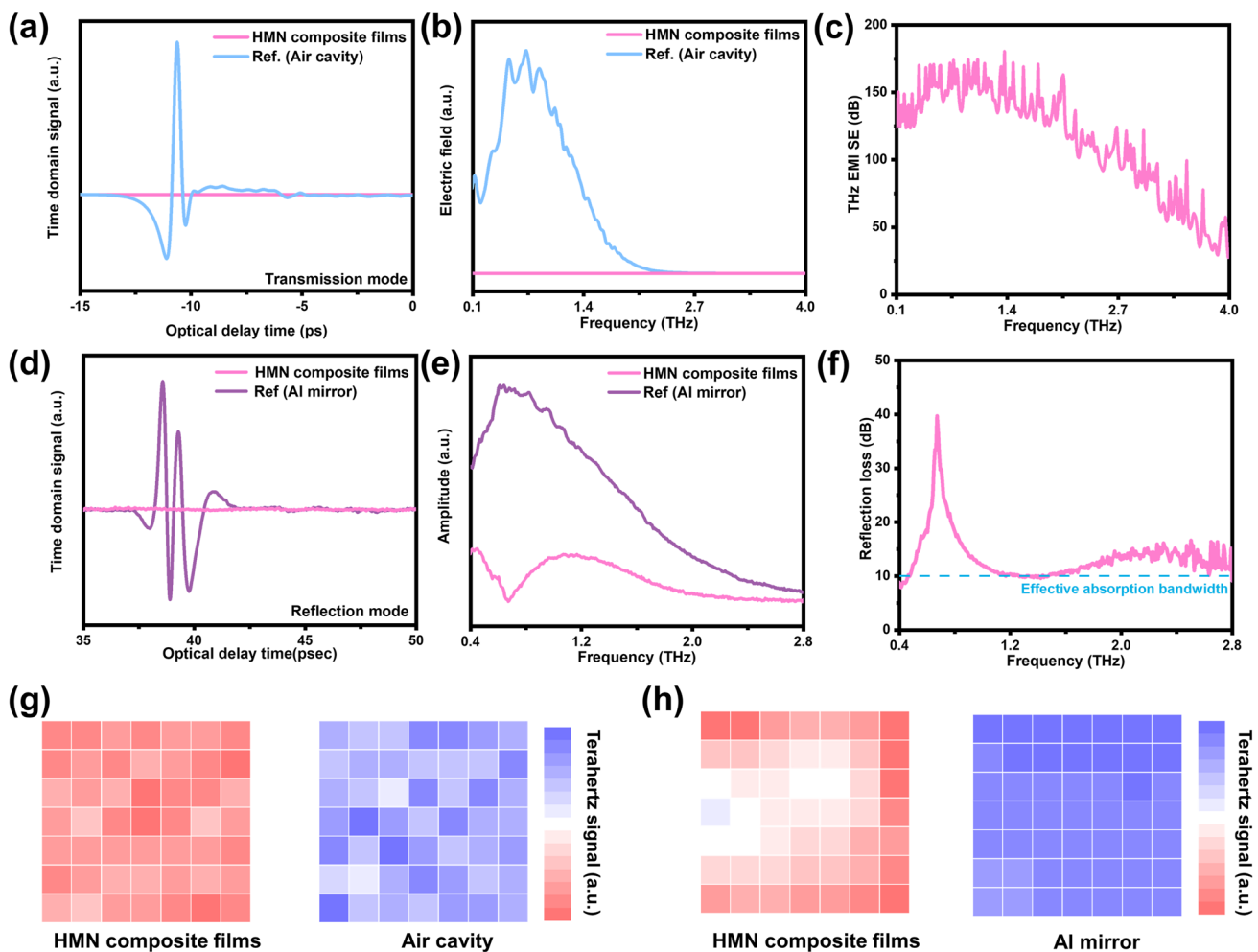


Fig. 5 Terahertz electromagnetic shielding performances of HMN composite films. **a, d** THz time domain pulses for air, Al mirror, and HMN composite films in transmission model and reflection model. **b, e** Electric field intensity for air, Al plate, and HMN composite films in transmission model and reflection model. **c, f** EMI SE and reflection loss of HMN composite films in transmission model and reflection model. **g, h** Terahertz imaging thermogram of transmission mode and reflection mode

composite films is depicted in Fig. 6e. The EMI shielding performance generally depends on mobile carriers, electric/magnetic dipoles, and internal interfaces [55]. Conductive loss is primarily caused by the movement and jumping of free electrons in the conductive channel [56, 57]. The conductivity component plays a pivotal role in influencing the electromagnetic shielding capabilities through the generation of a larger number of free charges [46]. Additionally, the asymmetric distribution of charges within materials can lead to dipole polarization. Materials with asymmetric charge distribution form dipoles that interact with the magnetic field. This interaction leads to the loss of electromagnetic waves. Dipole polarization leads to better EMI

shielding performance [58]. Furthermore, magnetic components can dissipate electromagnetic waves through the hysteresis loss, eddy current loss, domain wall resonance, ferromagnetic resonance, and natural resonance mechanisms [59, 60]. Under an alternating magnetic field, electrons will undergo spin motion and cause resonance between the magnetic filler and the magnetic field, resulting in the loss of electromagnetic waves [61]. When electromagnetic waves are incident from the initial layer of the HMN composite films, there will be losses resulting from scattering and absorption by the TOCNFs/Co-HCC with the mechanism of magnetic loss and dielectric loss. Furthermore, the highly graphitized out shell carbon framework present in

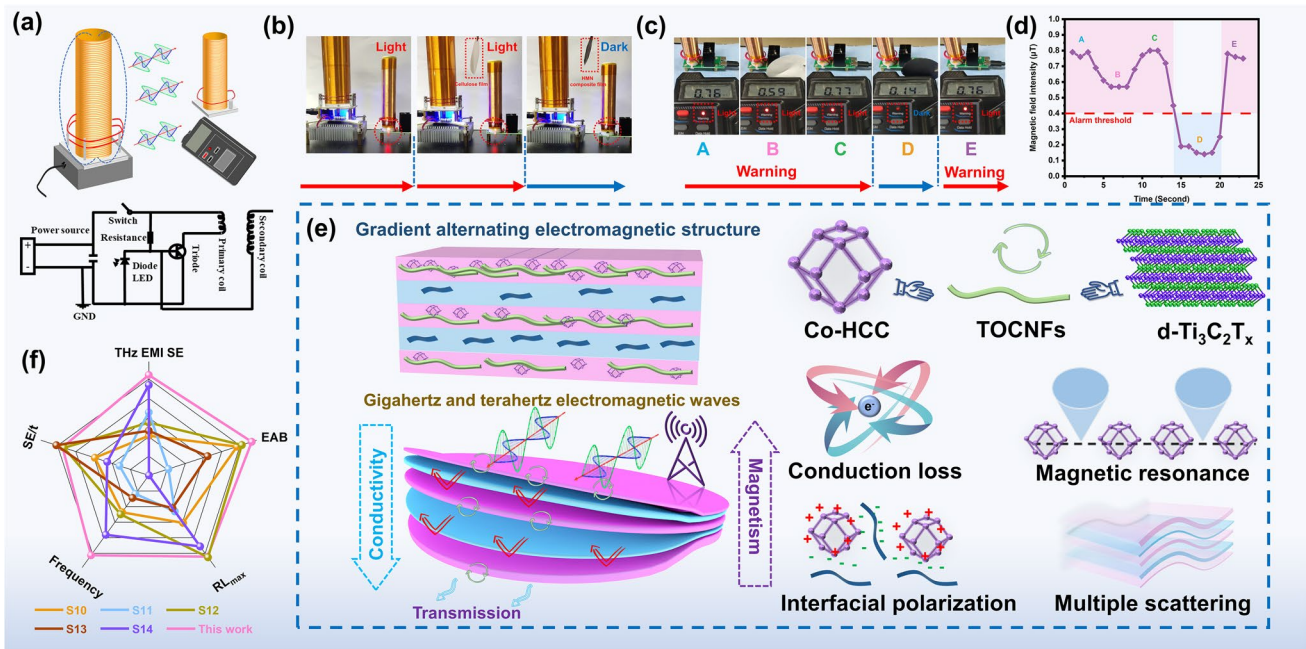


Fig. 6 EMI simulated visually and EMI shielding mechanism. **a** Schematic diagram of the EMI simulated visually and Tesla coil circuit diagram. **b** Tesla coil experiment of HMN composite films. **c** Electromagnetic shielding detector EMI performance and **d** experiment of HMN composite films. **e** Schematic diagram of the EMI shielding mechanism of HMN composite films. **f** Comparison of the EMI SE with other materials (sample numbers listed in Table S2 in Supporting Information)

Co-HCC also forms the conductive pathway and abundant heterogeneous interfaces, further enhancing the loss of electromagnetic waves [62]. When the residual electromagnetic wave passes through the initial layer to the next layer, part of the electromagnetic wave is lost due to interfacial polarization. Another part is reflected to the initial layer or converted into heat energy due to the conductivity loss of d-Ti₃C₂T_x. The electromagnetic wave transmitted through the first and two layers will contact the third layer again and then be absorbed or reflected again. The remaining electromagnetic waves will re-enter the subsequent layer and continue to be dissipated. Notably, the gradient electromagnetic alternating structure effectively utilizes the respective advantages of electromagnetic components to enhance the loss ability of electromagnetic waves. Additionally, with the gradient positive sequence increase of d-Ti₃C₂T_x and gradient backward sequence increase content of TOCNFs/Co-HCC, more electromagnetic waves are absorbed in the front layers and reflected in the back layers, thus achieving the advantage of improving the EMI SE and realize the optimization of electromagnetic components. The intermittent and gradient conductive network is beneficial

to improve the electromagnetic shielding performance of materials [63]. On the contrary, due to the disordered distribution of electromagnetic components, materials with random structures cannot form an effective electromagnetic wave loss network. Lack of an organized structure also leads to a loss of the ability to reflect and absorb the energy, resulting in a low level of electromagnetic shielding [64]. Hence, the design of the structure will produce gradient impedance matching, and the multi-layer structure introduced will cause extra electromagnetic energy loss at the corners generated by electromagnetic waves [65, 66]. The comparison of the EMI SE with other materials is displayed in Fig. 6f and Table S1.

3.4 Photothermal Conversion Performances and Applicability of HMN Composite Films

Deriving from the local surface plasmon resonance (LSPR) effect for solar radiation, MXene and MOFs have efficient light-to-heat conversion capability [67, 68]. MXene/MOFs functional materials have been widely used in photothermal

conversion devices. The light absorption performance of materials is one of the important factors affecting photothermal conversion. As displayed in Fig. 7a, the absorption spectra of HMN composite films at all solar wavelengths were measured by UV–Vis–NIR spectrophotometer. The absorption capacity of HMN composite film shows a high level in the whole wavelength range, which proves its strong absorption capacity. As shown in Fig. 7b, d, HMN composite films exhibited high solar thermal conversion performance.

Under the irradiation of 0.5, 1, 1.5, and 2.0 Sun (1 Sun = 1 KW m⁻²), the surface temperature of HMN-5L-57.1% rapidly reached to 48.6, 73.2, 84.1, and 104.6 °C, respectively. Besides, the solar response ability and cyclic response ability are displayed in Fig. 7c. After the simulated sunlight was turned off, the surface temperature of HMN composite films rapidly decreased. Even after repeated three cycles, it still maintains good solar conversion ability. Furthermore, given that the NIR laser possesses a higher power density, it can be

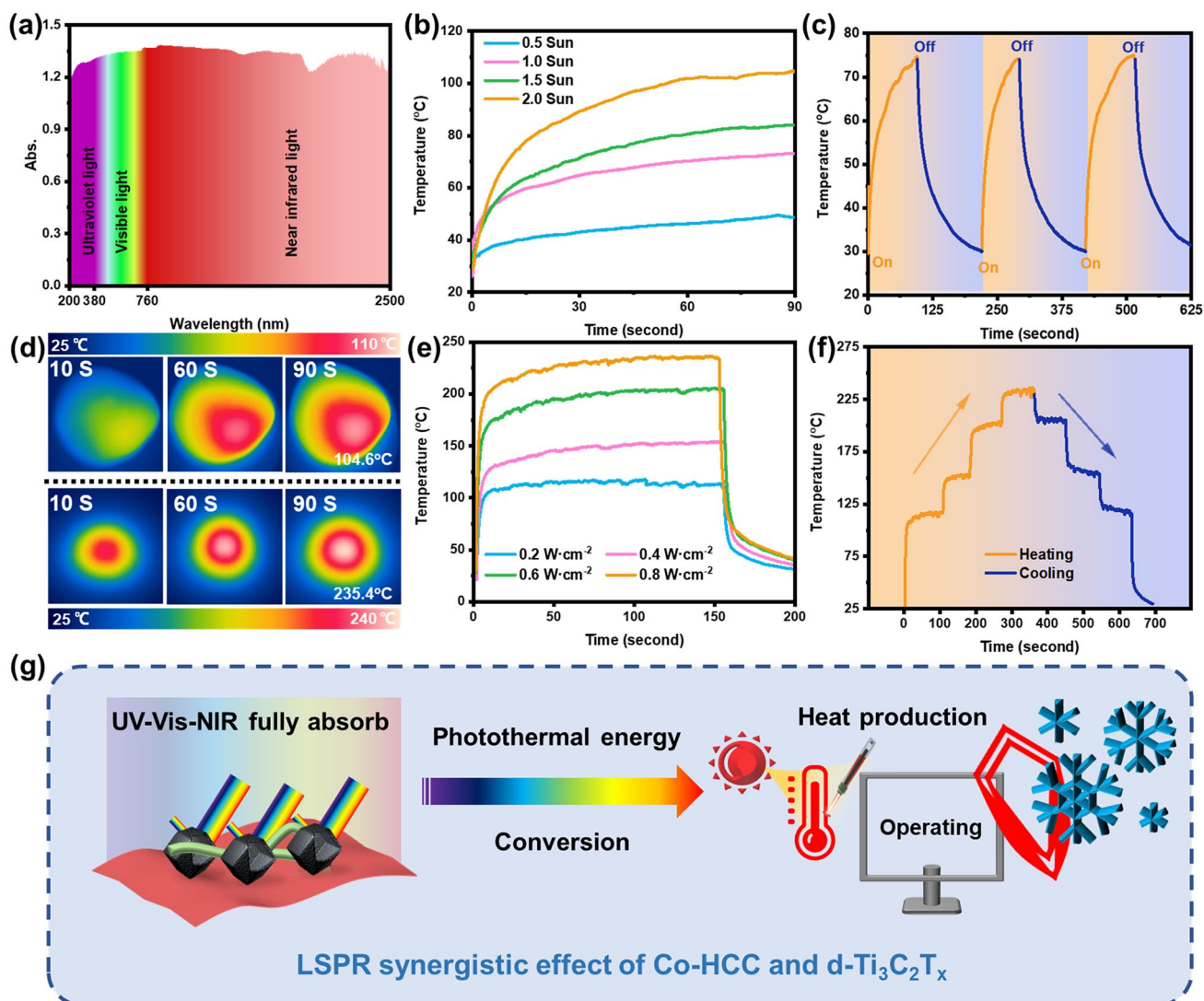


Fig. 7 Photothermal conversion performances of HMN composite films. **a** UV–Vis–NIR absorbance spectrum of HMN composite films. **b** Surface temperature curves for the HMN composite films under different solar intensity. **c** Solar-heating performance of HMN composite films in 3 cycles with an applied solar intensity of 1.0 Sun. **d** Infrared thermographic photographs of HMN composite films under 2.0 Sun (upper) and NIR irradiation (lower) under 0.8 W cm⁻² at different time intervals. **e** Surface temperature curves for the HMN composite films under different 808 NIR power densities. **f** Temperature evolution of HMN composite films at different 808 NIR laser power densities. **g** Schematic diagram of HMN composite films irradiated by simulant photothermal

used to quickly raise the photothermal material to a higher temperature in a shorter time. The NIR laser irradiation thermal conversion performance of HMN composite films was investigated. As shown in Fig. 7d, e, the HMN-5L-57.1% displayed obvious temperature gradient changes with different NIR laser irradiation intensity proportions from 0.2 to 0.8 W cm⁻². The highest surface temperature can reach 235.4 °C under 0.8 W cm⁻². Furthermore, through the alternating state of temperature rise/fall and repeated light on/off with different radiation intensity, the stability of NIR laser irradiation thermal conversion of HMN-5L-57.1% was confirmed (Fig. 7f). Temperature evolution processes of HMN-5L-57.1% were stable during different NIR laser power densities irradiation. Besides, the highest surface temperature and temperature rise rate curve of HMN composite films are basically consistent under 20 consecutive cycles of on/off and long-term illumination, and it has more cycles of on/off ability and continuous heating time than previously reports (Figs. S21, S22 and Table S3). The solar-to-thermal conversion efficiency of the HMN composite films was measured. Due to ultra-high light absorption rate and low near-infrared emissivity, the photothermal conversion efficiency of HMN composite films can reach 66.2% (Figs. S23 and S24). CNT derived from the surface of Co-HCC endows nanoparticles with a rougher surface, which is beneficial to generate more hot spots, thus improving the photothermal conversion ability of materials. In addition, LSPR is further promoted in the hollow structure and heat loss can be reduced. The hierarchical structure and the LSPR synergistic effect of d-siTi₃C₂T_x and Co-HCC endow HMN composite films with excellent photothermal conversion on ability (Fig. 7g) [69].

With the miniaturization and precision of electronic equipment, integrated multifunctional electromagnetic shielding materials need to be light, thin, and flexible. As shown in Fig. S25a, HMN composite films have the characteristics of low density (placed on dandelion fluff without collapse), ultra-thin (the thickness is only ~0.2 mm), and flexible (bent on the glass rod without crack). In addition, through cutting, HMN composite film can be cut into any shape to meet a variety of personalized needs (Fig. S25b). Besides, the mechanical performance of HMN composite films was further investigated. The good flexibility of HMN composite films can endow it with the property that it can withstand bending at different angles without breaking (Fig. S26). The typical tensile stress–strain curves are shown in Fig. S27. The ultimate strengths of the d-Ti₃C₂T_x,

TOCNF, and HMN composite films are about 2.7, 14.3, and 18.7 MPa, respectively. Additionally, the tensile strain percentage of the d-Ti₃C₂T_x, TOCNF, and HMN composite films is about 1.0%, 5.5%, and 4.8%. The mechanical properties are helpful to improve the adaptability of electromagnetic shielding materials in various application scenarios [70]. Interestingly, because Co-HCC nanoparticles have high magnetism, they can be easily attracted by magnets without falling off. This is beneficial to be attached to the surface of devices or implanted in magnetic fabrics in the future (Fig. S28 and Movie S3). Moreover, due to the design of the multi-layer structure, the d-Ti₃C₂T_x layer is protected by the outer TOCNFs/Co-HCC layer, and the HMN composite films can be kept intact in the 180-W ultrasonic process, while the pure d-Ti₃C₂T_x films were quickly dissolved in water within 30 s. Hydrogen bonding and physical entanglement between TOCNFs endow HMN composite films with moisture resistance (Fig. S29) [71].

4 Conclusions

In summary, we prepared hollow MOFs/layered MXene/nanocellulose composite films with alternating electromagnetic structures via macro/micro–electromagnetic structural design. The HMN composite films are applied for ultra-wideband giga/terahertz electromagnetic shielding and photothermal conversion. The HMN composite films displayed excellent EMI shielding effectiveness (EMI SE) performance in the GHz frequency (average 66.8 dB at Ka-band) and THz frequency (average 114.6 dB at 0.1–4.0 THz). Besides, the HMN composite films also exhibit a high reflection loss of 39.7 dB at 0.7 THz with an effective absorption bandwidth up to 2.1 THz. Moreover, the electromagnetic shielding application of HMN composite film is proved by simulating and visualizing the electromagnetic shielding application. Furthermore, HMN composite films show remarkable solar/laser photothermal conversion performance, which can reach 104.6 °C under 2.0 Sun and 235.4 °C under 0.8 W cm⁻², respectively. Therefore, the HMN composite films with structural design will be highly promising for a promising candidate for advanced EMI devices for future 6G electronic communication and the protection of electronic equipment in cold environments.

Acknowledgements The financial support from the Beijing Nova Program (20230484431) and Opening Project of State Silica-Based

Materials Laboratory of Anhui Province (2022KF12) is gratefully acknowledged.

Declarations

Conflict of interests The authors declare that they have no known competing financial interests or personal relationships that could have appeared to influence the work reported in this paper.

Open Access This article is licensed under a Creative Commons Attribution 4.0 International License, which permits use, sharing, adaptation, distribution and reproduction in any medium or format, as long as you give appropriate credit to the original author(s) and the source, provide a link to the Creative Commons licence, and indicate if changes were made. The images or other third party material in this article are included in the article's Creative Commons licence, unless indicated otherwise in a credit line to the material. If material is not included in the article's Creative Commons licence and your intended use is not permitted by statutory regulation or exceeds the permitted use, you will need to obtain permission directly from the copyright holder. To view a copy of this licence, visit <http://creativecommons.org/licenses/by/4.0/>.

Supplementary Information The online version contains supplementary material available at <https://doi.org/10.1007/s40820-024-01386-5>.

References

1. F. Shahzad, M. Alhabeab, C.B. Hatter, B. Anasori, S.M. Hong et al., Electromagnetic interference shielding with 2D transition metal carbides (MXenes). *Science* **353**, 1137–1140 (2016). <https://doi.org/10.1126/science.aag2421>
2. Z. Zeng, G. Wang, B.F. Wolan, N. Wu, C. Wang et al., Printable aligned single-walled carbon nanotube film with outstanding thermal conductivity and electromagnetic interference shielding performance. *Nano-Micro Lett.* **14**, 179 (2022). <https://doi.org/10.1007/s40820-022-00883-9>
3. C. Ma, Q. Yuan, M.-G. Ma, MXenes for electromagnetic interference (EMI) shielding. *Fundamental Aspects and Perspectives of MXenes*. (Springer, Cham, 2022), 219–240. https://doi.org/10.1007/978-3-031-05006-0_9
4. P.-L. Wang, T. Mai, X.-X. Ji, P. Hu, M.-G. Ma, Aerogel-based composites for electromagnetic interface shielding applications. *Compos. Interfaces* **29**, 1483–1503 (2022). <https://doi.org/10.1080/09276440.2022.2069320>
5. Z. Barani, F. Kargar, Y. Ghafouri, S. Ghosh, K. Godziszewski et al., Electrically insulating flexible films with quasi-1D van der Waals fillers as efficient electromagnetic shields in the GHz and sub-THz frequency bands. *Adv. Mater.* **33**, e2007286 (2021). <https://doi.org/10.1002/adma.202007286>
6. J. Wang, X. Wu, Y. Wang, W. Zhao, Y. Zhao et al., Green, sustainable architectural bamboo with high light transmission and excellent electromagnetic shielding as a candidate for energy-saving buildings. *Nano-Micro Lett.* **15**, 11 (2022). <https://doi.org/10.1007/s40820-022-00982-7>
7. Q. Lu, Y. Chen, W. Song, C. Tao, J. Zhang et al., Mechanistic role of γ -valerolactone co-solvent to promote ethyl levulinate production from cellulose transformation in ethanol. *Fuel* **346**, 128371 (2023). <https://doi.org/10.1016/j.fuel.2023.128371>
8. Z. Zhang, T. Yuan, Y. Miao, Q. Liu, J. Mu et al., Carboxyl-functionalized graphene oxide/cellulose nanofiber as adsorbents toward methylene blue. *Chem. Phys. Lett.* **837**, 141064 (2024). <https://doi.org/10.1016/j.cplett.2024.141064>
9. M. Naguib, M. Kurtoglu, V. Presser, J. Lu, J. Niu et al., Two-dimensional nanocrystals produced by exfoliation of Ti_3AlC_2 . *Adv. Mater.* **23**, 4248–4253 (2011). <https://doi.org/10.1002/adma.201102306>
10. F. Shahzad, A. Iqbal, H. Kim, C.M. Koo, 2D transition metal carbides (MXenes): applications as an electrically conducting material. *Adv. Mater.* **32**, e2002159 (2020). <https://doi.org/10.1002/adma.202002159>
11. M.M. Hasan, M.M. Hossain, H.K. Chowdhury, Two-dimensional MXene-based flexible nanostructures for functional nanodevices: a review. *J. Mater. Chem. A* **9**, 3231–3269 (2021). <https://doi.org/10.1039/D0TA11103A>
12. Z. Liu, J. Chen, M. Que, H. Zheng, L. Yang et al., 2D $\text{Ti}_3\text{C}_2\text{T}$ MXene/MOFs composites derived CoNi bimetallic nanoparticles for enhanced microwave absorption. *Chem. Eng. J.* **450**, 138442 (2022). <https://doi.org/10.1016/j.cej.2022.138442>
13. Y. Wang, Y. Yang, M. Miao, X. Feng, Carbon nanotube arrays@cobalt hybrids derived from metal-organic framework ZIF-67 for enhanced electromagnetic wave absorption. *Mater. Today Phys.* **35**, 101110 (2023). <https://doi.org/10.1016/j.mtphys.2023.101110>
14. H. Zhang, X.-Y. Zheng, R. Jiang, Z. Liu, W. Li et al., Research progress of functional composite electromagnetic shielding materials. *Eur. Polym. J.* **185**, 111825 (2023). <https://doi.org/10.1016/j.eurpolymj.2023.111825>
15. Y. Fei, M. Liang, Y. Chen, H. Zou, Sandwich-like magnetic graphene papers prepared with MOF-derived Fe_3O_4 -C for absorption-dominated electromagnetic interference shielding. *Ind. Eng. Chem. Res.* **59**, 154–165 (2020). <https://doi.org/10.1021/acs.iecr.9b04416>
16. Y. Liu, Y. Wang, N. Wu, M. Han, W. Liu et al., Diverse structural design strategies of MXene-based macrostructure for high-performance electromagnetic interference shielding. *Nano-Micro Lett.* **15**, 240 (2023). <https://doi.org/10.1007/s40820-023-01203-5>
17. W. Cao, C. Ma, S. Tan, M. Ma, P. Wan et al., Ultrathin and flexible CNTs/MXene/cellulose nanofibrils composite paper for electromagnetic interference shielding. *Nano-Micro Lett.* **11**, 72 (2019). <https://doi.org/10.1007/s40820-019-0304-y>
18. G. Hu, C. Wu, Q. Wang, F. Dong, Y. Xiong, Ultrathin nanocomposite films with asymmetric gradient alternating multilayer structures exhibit superhigh electromagnetic interference shielding performances and robust mechanical properties. *Chem. Eng. J.* **447**, 137537 (2022). <https://doi.org/10.1016/j.cej.2022.137537>

19. Y. Pan, K. Sun, S. Liu, X. Cao, K. Wu et al., Core-shell ZIF-8@ZIF-67-derived CoP nanoparticle-embedded N-doped carbon nanotube hollow polyhedron for efficient overall water splitting. *J. Am. Chem. Soc.* **140**, 2610–2618 (2018). <https://doi.org/10.1021/jacs.7b12420>
20. Z. Xiang, X. Wang, X. Zhang, Y. Shi, L. Cai et al., Self-assembly of nano/microstructured 2D Ti_3CNT_x MXene-based composites for electromagnetic pollution elimination and Joule energy conversion application. *Carbon* **189**, 305–318 (2022). <https://doi.org/10.1016/j.carbon.2021.12.075>
21. Z.H. Zeng, N. Wu, J.J. Wei, Y.F. Yang, T.T. Wu et al., Porous and ultra-flexible crosslinked MXene/polyimide composites for multifunctional electromagnetic interference shielding. *Nano-Micro Lett.* **14**, 59 (2022). <https://doi.org/10.1007/s40820-022-00800-0>
22. Y. Xu, Z. Lin, K. Rajavel, T. Zhao, P. Zhu et al., Tailorable, lightweight and superelastic liquid metal monoliths for multifunctional electromagnetic interference shielding. *Nano-Micro Lett.* **14**, 29 (2021). <https://doi.org/10.1007/s40820-021-00766-5>
23. Z. Huang, H. Chen, S. Xu, L.Y. Chen, Y. Huang et al., Graphene-based composites combining both excellent terahertz shielding and stealth performance. *Adv. Opt. Mater.* **6**, 1801165 (2018). <https://doi.org/10.1002/adom.201801165>
24. P.-L. Wang, T. Mai, W. Zhang, M.-Y. Qi, L. Chen et al., Robust and multifunctional $\text{Ti}_3\text{C}_2\text{T}_x$ modified sawdust composite paper for electromagnetic interference shielding and wearable thermal management. *Small* **20**, e2304914 (2024). <https://doi.org/10.1002/sml.202304914>
25. Y. Sun, H. Jia, J. Liu, H. Yu, X. Jiang, Metal-organic framework-derived C/Co/Co₃O₄ nanocomposites with excellent microwave absorption properties in low frequencies. *J. Mater. Sci. Mater. Electron.* **31**, 11700–11713 (2020). <https://doi.org/10.1007/s10854-020-03721-z>
26. R. Qiang, Y. Du, D. Chen, W. Ma, Y. Wang et al., Electromagnetic functionalized Co/C composites by *in situ* pyrolysis of metal-organic frameworks (ZIF-67). *J. Alloys Compd.* **681**, 384–393 (2016). <https://doi.org/10.1016/j.jallcom.2016.04.225>
27. P. Yin, T. Yao, Y. Wu, L. Zheng, Y. Lin et al., Single cobalt atoms with precise N-coordination as superior oxygen reduction reaction catalysts. *Angew. Chem. Int. Ed.* **55**, 10800–10805 (2016). <https://doi.org/10.1002/anie.201604802>
28. Y. Fan, C. Zhuang, S. Li, Y. Wang, X. Zou et al., Efficient single-atom Ni for catalytic transfer hydrogenation of furfural to furfuryl alcohol. *J. Mater. Chem. A* **9**, 1110–1118 (2021). <https://doi.org/10.1039/D0TA10838C>
29. B.Y. Xia, Y. Yan, N. Li, H.B. Wu, X.W. Lou et al., A metal-organic framework-derived bifunctional oxygenelectrocatalyst. *Nat. Energy* **1**, 15006 (2016). <https://doi.org/10.1038/nenergy.2015.6>
30. Y. Fan, S. Li, Y. Wang, C. Zhuang, X. Liu et al., Tuning the synthesis of polycyclic-doped ZIF derived materials for efficient hydrogenation of furfural to furfuryl alcohol. *Nanoscale* **12**, 18296–18304 (2020). <https://doi.org/10.1039/d0nr04098c>
31. C. Ma, T. Mai, P.-L. Wang, W.-Y. Guo, M.-G. Ma, Flexible MXene/nanocellulose composite aerogel film with cellular structure for electromagnetic interference shielding and photothermal conversion. *ACS Appl. Mater. Interfaces* **15**, 47425–47433 (2023). <https://doi.org/10.1021/acsami.3c12171>
32. H. Cheng, Y. Pan, X. Wang, C. Liu, C. Shen et al., Ni flower/MXene-melamine foam derived 3D magnetic/conductive networks for ultra-efficient microwave absorption and infrared stealth. *Nano-Micro Lett.* **14**, 63 (2022). <https://doi.org/10.1007/s40820-022-00812-w>
33. T. Mai, P.-L. Wang, Q. Yuan, C. Ma, M.-G. Ma, *In situ* anchoring Zn-doped ZIF-67 on carboxymethylated bacterial cellulose for effective indigo carmine capture. *Nanoscale* **13**, 18210–18217 (2021). <https://doi.org/10.1039/d1nr05388d>
34. Z. Guang, Y. Huang, C. Chen, X. Liu, Z. Xu et al., Engineering a light-weight, thin and dual-functional interlayer as “polysulfides sieve” capable of synergistic adsorption for high-performance lithium-sulfur batteries. *Chem. Eng. J.* **383**, 123163 (2020). <https://doi.org/10.1016/j.cej.2019.123163>
35. E. Duraisamy, H.T. Das, A. Selva Sharma, P. Elumalai, Supercapacitor and photocatalytic performances of hydrothermally-derived Co₃O₄/CoO@carbon nanocomposite. *New J. Chem.* **42**, 6114–6124 (2018). <https://doi.org/10.1039/C7NJ04638C>
36. M.-Y. Qi, P.-L. Wang, L.-Z. Huang, Q. Yuan, T. Mai et al., Cellulose nanofiber/MXene/luffa aerogel for all-weather and high-efficiency cleanup of crude oil spills. *Int. J. Biol. Macromol.* **242**, 124895 (2023). <https://doi.org/10.1016/j.ijbiomac.2023.124895>
37. L. Luo, Z. Fang, W. Zhang, S. Geng, B. Chen et al., Preparation of methylated TEMPO-oxidized cellulose nanofibril hydrogel with high-temperature sensitivity. *Cellulose* **29**, 8599–8609 (2022). <https://doi.org/10.1007/s10570-022-04811-3>
38. T. Mai, W.Y. Guo, P.L. Wang, L. Chen, M.Y. Qi et al., Bilayer metal-organic frameworks/MXene/nanocellulose paper with electromagnetic double loss for absorption-dominated electromagnetic interference shielding. *Chem. Eng. J.* **464**, 142517 (2023). <https://doi.org/10.1016/j.cej.2023.142517>
39. Q.-W. Wang, H.-B. Zhang, J. Liu, S. Zhao, X. Xie et al., Multifunctional and water-resistant MXene-decorated polyester textiles with outstanding electromagnetic interference shielding and joule heating performances. *Adv. Funct. Mater.* **29**, 1806819 (2019). <https://doi.org/10.1002/adfm.201806819>
40. S.A. Al Kiey, H.N. Abdelhamid, Metal-organic frameworks (MOFs)-derived Co₃O₄@N-doped carbon as an electrode materials for supercapacitor. *J. Energy Storage* **55**, 105449 (2022). <https://doi.org/10.1016/j.est.2022.105449>
41. Z. Zhang, D. Li, J. Wang, J. Jiang, Cascade upcycling polystyrene waste into ethylbenzene over Fe₂N@C. *Appl. Catal. B Environ.* **323**, 122164 (2023). <https://doi.org/10.1016/j.apcatb.2022.122164>
42. D.-D. Li, Q. Yuan, L.-Z. Huang, W. Zhang, W.-Y. Guo et al., Preparation of flexible N-doped carbon nanotube/MXene/PAN nanocomposite films with improved electrochemical properties. *Ind. Eng. Chem. Res.* **60**, 15352–15363 (2021). <https://doi.org/10.1021/acs.iecr.1c03182>



43. N. Jia, D. Li, G. Huang, J. Sun, P. Lu et al., Carbon fibers-coated Co@N-doped porous carbon derived from ZIF-67/alginate fibers for efficient oxygen reduction reaction. *J. Photonics Energy* **10**(2), 023507 (2020). <https://doi.org/10.1117/1.JPE.10.023507>
44. S. Yi, X. Yue, D. Xu, Z. Liu, F. Zhao et al., Study on photogenerated charge transfer properties and enhanced visible-light photocatalytic activity of p-type Bi₂O₃/n-type ZnO heterojunctions. *New J. Chem.* **39**, 2917–2924 (2015). <https://doi.org/10.1039/C4NJ01738B>
45. W. Yang, Z. Zhao, K. Wu, R. Huang, T. Liu et al., Ultrathin flexible reduced graphene oxide/cellulose nanofiber composite films with strongly anisotropic thermal conductivity and efficient electromagnetic interference shielding. *J. Mater. Chem. C* **5**, 3748–3756 (2017). <https://doi.org/10.1039/C7TC00400A>
46. Y. Wang, W. Zhao, L. Tan, Y. Li, L. Qin et al., Review of polymer-based composites for electromagnetic shielding application. *Molecules* **28**, 5628 (2023). <https://doi.org/10.3390/molecules28155628>
47. X. Pei, G. Liu, H. Shi, R. Yu, S. Wang et al., Directional electromagnetic interference shielding of asymmetric structure based on dual-needle 3D printing. *Compos. Sci. Technol.* **233**, 109909 (2023). <https://doi.org/10.1016/j.compscitech.2023.109909>
48. S.M. Seyedi Ghezghapan, A. Javadi, Effect of processing methods on electrical percolation and electromagnetic shielding of PC/MWCNTs nanocomposites. *Polym. Compos.* **38**, E269–E276 (2017). <https://doi.org/10.1002/pc.24037>
49. B. Zhou, Z. Zhang, Y. Li, G. Han, Y. Feng et al., Flexible, robust, and multifunctional electromagnetic interference shielding film with alternating cellulose nanofiber and MXene layers. *ACS Appl. Mater. Interfaces* **12**, 4895–4905 (2020). <https://doi.org/10.1021/acsami.9b19768>
50. T. Xue, Y. Yang, D. Yu, Q. Wali, Z. Wang et al., 3D printed integrated gradient-conductive MXene/CNT/polyimide aerogel frames for electromagnetic interference shielding with ultra-low reflection. *Nano-Micro Lett.* **15**, 45 (2023). <https://doi.org/10.1007/s40820-023-01017-5>
51. B. Xue, Y. Li, Z. Cheng, S. Yang, L. Xie et al., Directional electromagnetic interference shielding based on step-wise asymmetric conductive networks. *Nano-Micro Lett.* **14**, 16 (2021). <https://doi.org/10.1007/s40820-021-00743-y>
52. X. Li, H. Luo, Maximizing terahertz energy absorption with MXene absorber. *Nano-Micro Lett.* **15**, 198 (2023). <https://doi.org/10.1007/s40820-023-01167-6>
53. A.R. Pai, Y. Lu, S. Joseph, N.M. Santhosh, R. Degl'Innocenti et al., Ultra-broadband shielding of cellulose nanofiber commingled biocarbon functional constructs: A paradigm shift towards sustainable terahertz absorbers. *Chem. Eng. J.* **467**, 143213 (2023). <https://doi.org/10.1016/j.cej.2023.143213>
54. H.M. Schlicke, Theory of simulated-skin-effect filters a thin film approach to EMI. *IEEE Trans. Electromagn. Compat.* **6**, 47–54 (1964). <https://doi.org/10.1109/TEM.1964.4307329>
55. B. Zhao, Y. Li, H. Ji, P. Bai, S. Wang et al., Lightweight graphene aerogels by decoration of 1D CoNi chains and CNTs to achieve ultra-wide microwave absorption. *Carbon* **176**, 411–420 (2021). <https://doi.org/10.1016/j.carbon.2021.01.136>
56. L. Ma, M. Hamidinejad, B. Zhao, C. Liang, C.B. Park, Layered foam/film polymer nanocomposites with highly efficient EMI shielding properties and ultralow reflection. *Nano-Micro Lett.* **14**, 19 (2021). <https://doi.org/10.1007/s40820-021-00759-4>
57. B. Zhao, Y. Du, Z. Yan, L. Rao, G. Chen et al., Structural defects in phase-regulated high-entropy oxides toward superior microwave absorption properties. *Adv. Funct. Mater.* **33**, 2209924 (2023). <https://doi.org/10.1002/adfm.202209924>
58. B. Zhao, Z. Yan, Y. Du, L. Rao, G. Chen et al., High-entropy enhanced microwave attenuation in titanate perovskites. *Adv. Mater.* **35**, e2210243 (2023). <https://doi.org/10.1002/adma.202210243>
59. B. Zhao, Z. Bai, H. Lv, Z. Yan, Y. Du et al., Self-healing liquid metal magnetic hydrogels for smart feedback sensors and high-performance electromagnetic shielding. *Nano-Micro Lett.* **15**, 79 (2023). <https://doi.org/10.1007/s40820-023-01043-3>
60. B. Zhao, S. Zeng, X. Li, X. Guo, Z. Bai et al., Flexible PVDF/carbon materials/Ni composite films maintaining strong electromagnetic wave shielding under cyclic microwave irradiation. *J. Mater. Chem. C* **8**, 500–509 (2020). <https://doi.org/10.1039/C9TC05462F>
61. C. Liang, Z. Gu, Y. Zhang, Z. Ma, H. Qiu et al., Structural design strategies of polymer matrix composites for electromagnetic interference shielding: A review. *Nano-Micro Lett.* **13**, 181 (2021). <https://doi.org/10.1007/s40820-021-00707-2>
62. D. Gao, S. Guo, Y. Zhou, B. Lyu, X. Li et al., Absorption-dominant, low-reflection multifunctional electromagnetic shielding material derived from hydrolysate of waste leather scraps. *ACS Appl. Mater. Interfaces* **14**, 38077–38089 (2022). <https://doi.org/10.1021/acsami.2c10787>
63. J.-R. Tao, X.-H. Tang, Q.-M. He, M. Wang, Effect of surface conductivity on electromagnetic shielding of multi-walled carbon nanotubes/Poly(ϵ -caprolactone) composites. *Compos. Sci. Technol.* **229**, 109715 (2022). <https://doi.org/10.1016/j.compscitech.2022.109715>
64. H. Wang, S. Li, M. Liu, J. Li, X. Zhou, Review on shielding mechanism and structural design of electromagnetic interference shielding composites. *Macromol. Mater. Eng.* **306**(6), 2100032 (2021). <https://doi.org/10.1002/mame.202100032>
65. S. Yang, R. Yang, Z. Lin, X. Wang, S. Liu et al., Ultrathin, flexible, and high-strength polypyrrole/Ti₃C₂T_x film for wide-band gigahertz and terahertz electromagnetic interference shielding. *J. Mater. Chem. A* **10**, 23570–23579 (2022). <https://doi.org/10.1039/D2TA06805B>
66. B. Zhao, R. Wang, Y. Li, Y. Ren, X. Li et al., Dependence of electromagnetic interference shielding ability of conductive polymer composite foams with hydrophobic properties on cellular structure. *J. Mater. Chem. C* **8**, 7401–7410 (2020). <https://doi.org/10.1039/D0TC00987C>
67. H. Liu, Z. Cui, L. Luo, Q. Liao, R. Xiong et al., Facile fabrication of flexible and ultrathin self-assembled Ti₃C₂T_x/bacterial cellulose composite films with enhanced electromagnetic shielding and photothermal conversion performances. *Chem.*

- Eng. J. **454**, 140288 (2022). <https://doi.org/10.1016/j.cej.2022.140288>
68. Y. Gao, J. Lin, X. Chen, Z. Tang, G. Qin et al., Engineering 2D MXene and LDH into 3D hollow framework for boosting photothermal energy storage and microwave absorption. *Small* **19**, e2303113 (2023). <https://doi.org/10.1002/sml.202303113>
69. S. Ding, L. Ma, J. Feng, Y. Chen, D. Yang et al., Surface-roughness-adjustable Au nanorods with strong plasmon absorption and abundant hotspots for improved SERS and photothermal performances. *Nano Res.* **15**, 2715–2721 (2022). <https://doi.org/10.1007/s12274-021-3740-1>
70. J. Ye, Y. Wang, L. Luo, K. Qian, J. Zhou et al., Carbon nanotube films embedded with Cu@C nanocubes for electromagnetic interference shielding. *J. Polym. Sci.* **61**, 2688–2696 (2023). <https://doi.org/10.1002/pol.20230184>
71. L. Chen, T. Mai, X.-X. Ji, P.-L. Wang, M.-Y. Qi et al., 3D printing of customizable and lightweight multilayer MXene/nanocellulose architectures for tunable electromagnetic interference shielding via direct ink writing. *Chem. Eng. J.* **476**, 146652 (2023). <https://doi.org/10.1016/j.cej.2023.146652>

